

1

Physics-dynamics coupling with element-based high-order Galerkin 2 methods: quasi equal-area physics grid

3 Adam R. Herrington*

4 *School of Marine and Atmospheric Sciences, Stony Brook University, Stony Brook, New York,
5 USA.*

6 Peter H. Lauritzen

7 *Climate and Global Dynamics, National Center for Atmospheric Research, 1850 Table Mesa
8 Drive, Boulder, Colorado, USA.*

9 Mark A. Taylor

10 *Sandia National Laboratories, Albuquerque, New Mexico, USA.*

11 Steve Goldhaber and Brian E. Eaton

12 *Climate and Global Dynamics, National Center for Atmospheric Research, 1850 Table Mesa
13 Drive, Boulder, Colorado, USA.*

14 Kevin A. Reed

15 *School of Marine and Atmospheric Sciences, Stony Brook University, State University of New
16 York, Stony Brook, New York.*

17 Paul A. Ullrich

¹⁸ Department of Land, Air and Water Resources, University of California, Davis, California, USA.

¹⁹ *Corresponding author address: Adam R. Herrington, School of Marine and Atmospheric Sciences, Stony Brook University, Stony Brook, New York, USA.

²⁰ E-mail: adam.herrington@stonybrook.edu

ABSTRACT

Atmospheric modeling with element-based high-order Galerkin methods presents a unique challenge to the conventional physics-dynamics coupling paradigm, due to the highly irregular distribution of nodes within an element and the distinct numerical characteristics of the Galerkin method. The conventional coupling procedure is to evaluate the physical parameterizations (*physics*) on the dynamical core grid. Evaluating the physics at the nodal points exacerbates numerical noise from the Galerkin method, enabling and amplifying local extrema at element boundaries. Grid imprinting may be substantially reduced through the introduction of an entirely separate, approximately isotropic finite-volume grid for evaluating the physics forcing. Integration of the spectral basis over the control-volumes provides an area average state to the physics, which is more representative of the state in the vicinity of the nodal points rather than the nodal point itself, and is more consistent with the notion of a ‘large-scale state’ required by conventional physics packages.

This study documents the implementation of a quasi-equal area physics grid into NCAR’s Community Atmosphere Model with Spectral Elements, and is shown to be effective at mitigating grid imprinting in the solution. The physics grid is also appropriate for coupling to other components within the Community Earth System Model, since the coupler requires component fluxes to be defined on a finite-volume grid, and one can be certain that the fluxes on the physics grid are indeed, volume-averaged.

43 **1. Introduction**

44 An increasing number of numerical methods publications in the atmospheric science literature
45 concern transport, shallow-water, and three-dimensional models employing element-based high-
46 order Galerkin discretizations such as finite-element and discontinuous Galerkin methods (for an
47 introduction to these methods see, e.g., Durran 2010; Nair et al. 2011; Ullrich 2014). Some global
48 models based on Galerkin methods have reached a level of maturity for which they are being con-
49 sidered for next generation climate and weather models due to their inherent conservation proper-
50 ties, high-order accuracy (for smooth problems), high parallel efficiency, high processor efficiency,
51 and geometric flexibility facilitating mesh-refinement applications. NCAR’s Community Atmo-
52 sphere Model (CAM; Neale et al. 2012) offers a dynamical core based on continuous Galerkin
53 finite elements (Taylor and Fournier 2010), referred to as CAM-SE (CAM Spectral Elements;
54 Taylor et al. 2008; Dennis et al. 2012; Lauritzen et al. 2018). CAM-SE is, in particular, being used
55 for high resolution climate modeling (e.g., Small et al. 2014; Reed et al. 2015; Bacmeister et al.
56 2018) and static mesh-refinement applications (e.g., Fournier et al. 2004; Zarzycki et al. 2014a,b;
57 Guba et al. 2014b; Rhoades et al. 2016). Other examples of models based on high-order Galerkin
58 methods that are being considered for ‘operational’ weather-climate applications are Giraldo and
59 Restelli (2008), Nair et al. (2009), Brdar et al. (2013) and E3SM (<https://e3sm.org/>).

60 Assumptions inherent to the physical parameterizations (also referred to as *physics*) require
61 the state passed by the dynamical core represent a ‘large-scale state’, for example, in quasi-
62 equilibrium-type convection schemes (Arakawa and Schubert 1974; Plant 2008). In finite-volume
63 methods (e.g., Lin 2004), one may think of the dynamical core state as the average state of the
64 atmosphere over a control volume, and for resolutions typical of climate simulations is entirely
65 consistent with the notion of a ‘large-scale state’. For finite-difference methods (e.g., Suarez et al.

66 1983) the point value is thought of as representative for the atmospheric state in the vicinity of the
67 point value and one can usually associate a volume with the grid-point. Hence the physics grid (the
68 grid on which the state of the atmosphere is evaluated and passed to physics) and the dynamics
69 grid (the grid the dynamical core uses) coincide. Having the physics and dynamics grids coin-
70 cide is obviously convenient since no interpolation is needed (which could disrupt conservation
71 properties) and the number of degrees of freedom on both grids is exactly the same.

72 For the regular latitude-longitude, cubed-sphere and icosahedral grids the distance between the
73 grid-points is gradually varying for finite-volume/finite-difference discretizations. Examples of
74 models that use these grids are CAM-FV (latitude-longitude grid, Lin 2004), FV3 (cubed-sphere
75 grid, Putman and Lin 2007) and ICON (icosahedral grid, Wan et al. 2013). For high-order
76 element-based Galerkin methods, the dynamical core grid is defined by the quadrature points. In
77 CAM-SE, these are the Gauss-Lobatto-Legendre (GLL) quadrature nodes. A unique aspect of the
78 high-order quadrature rules is that the nodes within an element are located at the roots of the basis
79 set, which may be irregularly spaced. For example, Figure 1 shows GLL points on an individual
80 element of a cubed-sphere grid for degree 3 ($np \times np = 4 \times 4$ quadrature points) and degree 7
81 ($np \times np = 8 \times 8$ quadrature points) Lagrange polynomial basis used in CAM-SE. The higher the
82 order of the quadrature rule, the greater variance in distance between GLL quadrature points within
83 an each element. GLL quadrature points cluster near the edges and, in particular, the corners of
84 the elements.

85 The resolved scales of motion are not determined by the distance between quadrature nodes,
86 but rather the degree of the polynomial basis in each element. The nodes may be viewed as
87 irregularly spaced samples of an underlying spectrally truncated state. From this perspective, one
88 might expect the nodal solutions to be independent of location within an element. While the
89 interior quadrature nodes are C^∞ in CAM-SE (i.e. the basis representation is infinitely smooth

and all derivatives are continuous), the smoothness of boundary nodes are constrained by the need to patch neighboring solutions together to form the global basis set, an operation known as the direct stiffness summation (DSS; Maday and Patera 1987; Canuto et al. 2007). The DSS operation is attractive because it allows for high-order accuracy with minimal communication between elements, but degrades the solution to C^0 at element boundaries (i.e., all derivatives are discontinuous). Through evaluating the physics at the nodal points, strong grid-scale forcing or oscillatory behavior near an element boundary may exacerbate the discontinuity, and our initial expectation, that the nodal solutions are independent of within-element location, is unlikely for non-smooth problems, e.g., the presence of rough topography or moist physics grid-scale forcing.

It is the purpose of this paper to document the implementation of an entirely separate, quasi-equal area finite-volume physics grid into CAM-SE. In this framework, the dynamical core state is integrated over control volumes to provide a volume averaged state to the physics, thereby minimizing the influence of any one particular nodal value on the physics forcing. Section 2 provides a thorough explanation of how grid imprinting manifests in high-order Galerkin methods for non-smooth problems. The implementation of the physics grid configuration into CAM-SE is presented in Section 3. Results from a hierarchy of idealized model configurations are presented in Section 4, illustrating the physics grid is effective at mitigating undesirable grid imprinting in the solution. Section 5 contains a discussion of results and concluding remarks.

2. The Quadrature Node Problem

Figure 2 is a schematic illustrating in one-dimension how grid-imprinting is enabled by the physics, when the dynamical core is built with high-order Galerkin methods. The schematic depicts a time-step, starting from smooth initial conditions (Figure 2a), and subsequently advancing the dynamics one Runge-Kutta time-step (Figure 2b). Since the boundary nodes of adjacent el-

ements overlap one-another, there are now two solutions for each boundary node. The DSS operator, effectively a numerical flux applied to the element boundaries such that overlapping nodal values agree, is applied (Figure 2c), degrading the boundary nodes to C^0 in the process. This discontinuity may be exacerbated if, e.g., the physics updates the state at an element boundary (Figure 2d,e), resulting in characteristically tighter gradients on the boundary nodes compared to if the physics forcing were applied to an interior node (Figure 2g,h).

To test the degree to which nodal solutions depend on within-element position, an aqua-planet simulation (Neale and Hoskins 2000; Medeiros et al. 2016), which consists of an ocean covered planet in perpetual equinox, with fixed, zonally symmetric sea surface temperatures idealized after the present day climatology, is carried out using CAM-SE, using CAM, version 4 physics (CAM4; Neale et al. 2010) and run for one year. The nominal low resolution *ne30np4* grid is used, pertaining to an average equatorial grid spacing of 111.2km. The probability density distribution of the upward vertical pressure velocity (ω), conditionally sampled based on three categories - ‘interior’, ‘edge’ and ‘corner’ nodes - is provided in Figure 3a. The rationale for concentrating on the ω field is that it closely follows divergent modes, which are sensitive to the discontinuous pressure gradients that characterize boundary nodes. There is an apparent dependence on nodal location, with interior nodes being characteristically sluggish, and corner and edge nodes having systematically larger magnitude vertical motion. This behavior is consistent with the smoothness properties of the different nodal locations, with discontinuous pressure gradients resulting in greater vertical motion at edge and corner nodes. The main division of solutions shown in Figure 3a is primarily between whether a node is, or is not situated on an element boundary, and is a nuanced signature of high-order element-based Galerkin methods for non-smooth problems.

If the conventional physics-dynamics coupling paradigm is applied to CAM-SE, then the physics are to be evaluated at the GLL nodes, and a volume associated with the quadrature point should

be defined. One approach to construct this grid is to decompose each spectral element into $(np - 1) \times (np - 1)$ subcells and then take the dual grid of this subcell grid. For cubed-sphere meshes, this dual grid will have a control volume associated with each quadrature point. These control volumes will be triangles for the cube corner quadrature points and quadrilaterals for all remaining quadrature points. Newton iteration can then be used to adjust the corners of these control volumes so that their spherical area exactly match the Gaussian weight multiplied by the metric term (these weights are used for integrating the basis functions over the elements and can therefore, in this context, be interpreted as areas). For cubed-sphere meshes, the Newton iteration can be replaced by a direct method if some of the quadrilaterals are replaced by pentagons giving additional flexibility in matching the spherical area to the quadrature weights. Such a dual grid is shown in Figure 4. This grid is used in the NCAR CESM (Community Earth System Model) coupler for passing states between ocean, atmosphere and land components since the current remapping method is finite-volume based and therefore requires control volumes (it is noted that methods exist that do not require control volumes for conservative interpolation, e.g., Ullrich and Taylor (2015)). Hence the components ‘see’ an irregular atmospheric grid. Similarly, the parameterizations in the atmosphere ‘see’ a state that is anisotropically sampled in space (see Figure 1 and 5 in Kim et al. 2008).

The quadrature grid in element-based Galerkin methods is defined to perform mathematical operations on the basis functions, e.g., computing gradients and integrals, rather than evaluating the state variables for physics-dynamics coupling. One may argue that it would be more consistent to integrate the basis functions over quasi-equal area control volumes within each element and pass those control volume average values to physics rather than irregularly spaced quadrature point values. In this case when integrating basis functions over control volumes a grid-cell average value is more representative of the values near the extrema at the element boundary than the quadrature

161 point value. The relationship between the nodal values, the basis functions and the proposed
162 control volumes is illustrated schematically in one-dimension in parts (f) and (i) in Figure 2.

163 **3. Methods**

164 Here we focus on CAM-SE, however, in principle the methods apply to any element-based high-
165 order Galerkin model. The physics grid in CAM-SE is defined by sub-dividing each element using
166 equi-angular gnomonic coordinate lines to define the sides of the physics grid control volumes (see
167 the Appendix for details). Note that the element boundaries are defined by equi-angular gnomonic
168 grid lines. The notation $pg = 3$ refers to the configuration where the elements are divided into
169 $pg \times pg = 3 \times 3$ equi-angular physics grid cells (see Figure 5) **resulting in a quasi-equal spherical**
170 **area grid**. Defining the physics grid by sub-dividing elements makes it possible to use the same el-
171 ement infrastructure as already used in CAM-SE, thereby facilitating its implementation. Here we
172 make use of the *ne30np4* and *ne30pg3* grids that use GLL quadrature point physics grid (physics
173 and dynamics grid coincide), and the same ($pg = 3$) resolution quasi equal-area physics grids, re-
174 spectively. In all configurations we use degree three Lagrange basis ($np = 4$) and $ne \times ne = 30 \times 30$
175 elements on each cubed-sphere panel.

176 A consequence of separating physics and dynamics grids is that the atmospheric state must be
177 mapped to the physics grid and the physics tendencies must be mapped back to the dynamics
178 grid. This is discussed in separate sections below. When separating physics and dynamics grids it
179 is advantageous to use a vertical coordinate that is static during physics-dynamics coupling. This
180 was one motivation to switch to a dry-mass vertical coordinate in CAM-SE (Lauritzen et al. 2018);
181 since dry mass remains constant throughout physics the dry-mass vertical coordinate remains fixed
182 during physics-dynamics coupling. **The dry mass coordinate subsequently evolves as floating**
183 **Lagrangian layers by the dynamics (Lin 2004) periodically mapped back to a reference hybrid-**

184 sigma-pressure coordinate after Simmons and Burridge (1981). All variables mapped between
185 grids are collocated, layer-mean values (Lauritzen et al. 2018).

186 *a. Mapping state from dynamics grid (GLL) to physics grid (pg)*

187 The dynamics state is defined on the GLL grid in terms of temperature $T^{(gll)}$, zonal wind com-
188 ponent $u^{(gll)}$, meridional wind component $v^{(gll)}$, and dry pressure level thickness $\Delta p^{(gll)}$. In the
189 mapping of the atmospheric state to the physics grid it is important that the following properties
190 are met:

- 191 1. conservation of scalar quantities such as mass and dry thermal energy,
- 192 2. for tracers; shape-preservation (monotonicity), i.e. the mapping method must not introduce
193 new extrema in the interpolated field, in particular, negatives,
- 194 3. consistency, i.e. the mapping preserves a constant,
- 195 4. linear correlation preservation.

196 Other properties that may be important, but not pursued here, includes total energy conservation
197 and axial angular momentum conservation; the main reason being that we did not manage to
198 construct a high-order reversible map that is consistent, shape-preserving and conservative. Also,
199 enforcing total energy conservation locally using, e.g. Lin (2004)'s method where total energy and
200 velocity components are remapped and temperature is a derived variable, has proven problematic
201 (C. Chen, personal communication).

202 We argue that the most consistent method for mapping scalar state variables from the GLL grid
203 to the physics grid is to integrate the Lagrange basis function representation (used by the SE dy-
204 namical core) over the physics grid control volumes, i.e. integrate the basis function representation
205 of $\Delta p^{(gll)} \times T^{(gll)}$ and $\Delta p^{(gll)}$ over the physics grid control volume (see, e.g., Lauritzen et al. 2017;

$$\Delta p^{(pg)} = \frac{1}{A^{(pg)}} \int_{A^{(pg)}} \Delta p^{(gll)} dA, \quad (1)$$

$$T^{(pg)} = \frac{1}{A^{(pg)} \Delta p^{(pg)}} \int_{A^{(pg)}} T^{(gll)} \Delta p^{(gll)} dA, \quad (2)$$

207 where $A^{(pg)}$ is the physics grid area. The integrals are numerically computed using the GLL
 208 quadrature rule which exactly (to machine precision) integrates the basis functions over the pg
 209 control volumes (Lauritzen et al. 2017). Thermal energy and dry air mass is conserved and the
 210 mapping is consistent. For the wind, which is a vector, the zonal and meridional wind components
 211 are mapped by transforming to contra-variant wind components, evaluating the basis function
 212 representation thereof at the equi-angular center of the physics grid control volumes and then
 213 transformed back to latitude-longitude coordinate system winds. All of the operations are local to
 214 the element and do not require communication between elements.

215 The mapping of tracers is more problematic since the SE basis function representation is oscil-
 216 latory although the shape-preserving filter guarantees shape-preservation at the GLL nodes (Guba
 217 et al. 2014a). To avoid this issue we use the CAM-SE-CSLAM version of CAM-SE (Conservative
 218 Semi-Lagrangian Multi-tracer transport scheme Lauritzen et al. 2017), where tracers are advected
 219 on the $pg = 3$ physics grid. Note that in CAM-SE-CSLAM the dry mass internally predicted by
 220 CSLAM, $\Delta p^{(cslam)}$, is, by design, equal to $\Delta p^{(gll)}$ integrated over the CSLAM/physics grid con-
 221 trol volume (Lauritzen et al. 2017). Since the tracer grid and physics grids are co-located and
 222 $\Delta p^{(pg)} = \Delta p^{(cslam)}$ then the mass conservation, correlation preservation, consistency and shape-
 223 preservation constraints are inherently fulfilled.

224 b. *Mapping tendencies from physics grid (pg) to dynamics grid (GLL)*

225 The physics tendencies are computed on the finite-volume physics grid and are denoted
226 $f_T^{(pg)}, f_u^{(pg)}, f_v^{(pg)}$, and $f_m^{(pg)}$. Note that dry air mass is not modified by physics and hence there
227 is no tendency for dry mass, $f_{\Delta p} \equiv 0$. Also, it is important to map tendencies and not state from
228 the physics grid to GLL grid otherwise one will get spurious tendencies from mapping errors when
229 the actual physics tendency is zero (unless a reversible map is used).

230 It is important that this process:

231 1. for tracers; mass tendency is conserved,

232 2. for tracers; in each tracer grid cell the mass tendency from physics must not exceed tracer
233 mass available in tracer grid cell (it is assumed that the physics tendency will not drive tracer
234 mixing ratio negative on the physics grid),

235 3. linear correlation preservation,

236 4. consistency, i.e. the mapping preserves a constant tendency.

237 Other properties that may be important, but not pursued here, includes total energy conservation
238 (incl. components of total energy) and axial angular momentum conservation. Scalar variables
239 are mapped from **the** physics grid to GLL grid using a tensor-product Lagrange interpolation **in**
240 **two dimensions (i.e. we assume that the pressure variations in the vertical are small)**. The local
241 coordinates on a cubed-sphere are discontinuous at the element edges so the interpolation requires
242 special attention at the cube corners and edges. The details are provided in the Appendix. Lagrange
243 interpolation preserves a constant (including zero) and linear correlations. Tracer and physics grids
244 are co-located so tracer mass, tracer shape, and tracer correlations are trivially preserved on the
245 tracer grid; and the inconsistency in point 2 above will not appear.

246 Mapping from pg to GLL grids while conserving mass was found to be difficult without ex-
247 cessive grid imprinting at element edges. Mass-conservation (using conventional finite-volume
248 methods) requires a control volume to be defined around the GLL points (see, .e.g., Figure 4 in
249 this paper or Figure 8b in Ullrich et al. 2016). These volumes are artificial and not consistent with
250 the SE method. Integrating the CSLAM reconstruction of water tracers of such artificial control
251 volumes led to GLL node grid imprinting in the mapping and will not preserve a constant mixing
252 ratio since the mapping of $\Delta p^{(pg)}$ to GLL will not yield the GLL node value for dry pressure-level
253 thickness (i.e. the maps are not reversible).

254 It was also found important to use an interpolator that is smooth across element boundaries.
255 Using an algorithm that only uses information from an element of control volumes will (at best)
256 be C^0 at the element boundaries and therefore lead to boundary node grid imprinting. A stencil
257 that extends beyond one element is therefore necessary. After much experimentation, the best
258 results in terms of grid-imprinting were obtained with tensor-cubic interpolation and by using the
259 CAM-SE-CSLAM configuration (which requires the same boundary exchange/communication as
260 used in CSLAM).

261 *c. Time splitting and physics-dynamics coupling*

262 The physics and dynamics are integrated in time using a sequential-update approach (e.g.,
263 Williamson 2002). The dynamical core is sub-cycled over the (usually) longer physics time-step,
264 Δt_{phys} , e.g., the vertical remapping time-step Δt_{remap} is cycled $rsplit$ times, summing to Δt_{phys} . In
265 CAM-SE, a fraction of the physics forcing, e.g., $f_q \times \Delta t_{remap}$ is applied at the beginning of each
266 $rsplit$ vertical remap subcycles, such that the full forcing ($f_q \times \Delta t_{phys}$) is realized over the course
267 of a physics time-step. This approach of dribbling the tendencies over sub-intervals has the ad-
268 vantage of reducing gravity wave noise (Thatcher and Jablonowski 2016), but may disrupt tracer

269 mass conservation (Zhang et al. 2017). In CAM-SE-CSLAM, all but the tracer mass quantities are
270 dribbled, with tracer mass receiving the full physics update, e.g., $f_q \times \Delta t_{phys}$, applied only at the
271 beginning of the first remap sub-cycle, and thereby conserving tracer mass. This is the $f_{type} = 2$
272 configuration described in detail in Section 3.6.3 in Lauritzen et al. (2018).

273 In the SE integration of the equations of motion on the GLL grid the water species are
274 needed in the computation of the pressure gradient force and generalized expressions for heat
275 capacity at constant pressure c_p , etc. Hence the mixing ratios for water vapor and dynamical-
276 thermodynamically active condensates (e.g., cloud ice, cloud liquid, ...) are needed on the
277 GLL grid. We have chosen to advect the water species on the GLL grid using the SE method as
278 well as on the physics grid using CSLAM. Every time physics updates the water species on the
279 CSLAM grid, a forcing term (equal to the difference between updated CSLAM water variables and
280 the SE values) is applied to the GLL water variables using dribbling so that the CSLAM solution
281 and SE solution for water species are tightly coupled.

282 4. Results

283 A hierarchy of idealized model configurations are presented in order to elucidate the differ-
284 ences between CAM-SE and CAM-SE-CSLAM (available from the CESM2.1 release; <https://doi.org/10.5065/D67H1H0V>). Here, the configurations are presented in order of increas-
285 ing complexity, each with a pair of approximately 1° simulations, pertaining to the *ne30np4* and
286 *ne30pg3* grids, and a $\Delta t_{phys} = 1800$ s.
287

288 a. *Moist Baroclinic Wave*

289 The moist baroclinic wave test case was developed as part of the ‘CESM Simple Models’ project
290 (Polvani et al. 2017), and included in the release of CESM2. It is effectively the dry test-case of

291 Ullrich et al. (2014), but initialized with moisture and coupled to the Kessler moist physics routine
292 (Kessler 1969). For more details on this test case (which was part of the 2016 Dynamical Core
293 Model Intercomparison Project, see Ullrich et al. 2017), see Section 4.1 in Lauritzen et al. (2018).
294 A measure of the uncertainty of the reference solution, the L_2 difference norm between two high-
295 resolution solutions using different dynamical cores, was also presented in Lauritzen et al. (2018)
296 and provided again here in Figure 6. The L_2 norm between CAM-SE and CAM-SE-CSLAM lies
297 below the uncertainty of the reference solution, indicating their differences are insignificant.

298 The flow field of the baroclinic wave test is used to drive the terminator "toy"-chemistry test
299 of Lauritzen et al. (2015b). The terminator test is used to assess the tracer mass conservation
300 properties for linear-correlated reactive species being advected across the terminator line. The
301 model is initialized with two species for which their total mass is constant everywhere (constant
302 surface pressure and constant mixing ratio 4×10^{-6} kg/kg), such that if tracer mass is conserved,
303 then the column integrated sum of the species should not vary in time. Figure 7 provides a snapshot
304 of the mass-weighted, vertically integrated tracer mass at day 15. In CAM-SE, the tracer mass is
305 not conserved by day 15 and the field is populated by overshoots and undershoots. In contrast, by
306 day 15, CAM-SE-CSLAM still conserves tracer mass to within machine precision, consistent with
307 the previous results of this test-case initialized with a dry baroclinic wave (Lauritzen et al. 2017).

308 *b. Aqua-planets*

309 Two year long aqua-planet simulations are performed using CAM-SE and CAM-SE-CSLAM,
310 using the CAM4 physics package (Neale et al. 2010), as discussed in Section 2. Away from the
311 grid-scale, the mean states in the two models are very similar. Figure 8 shows the zonal-mean cli-
312 matological precipitation rates in CAM-SE and CAM-SE-CSLAM. Considering how sensitive this

313 aqua-planet configuration is to design choices in CAM-SE (Lauritzen et al. 2018), it is somewhat
314 unexpected that the zonal means look so similar to one another.

315 A plot similar to Figure 3a is constructed for the CAM-SE-CSLAM simulation, a probability
316 density distribution of upward ω conditionally sampled based on location within the element. Like
317 Figure 3a, Figure 3b divides up the control volumes by corner, edge and interior cells. Through the
318 use of the quasi-equal area physics grid, the dynamical core state appears more or less independent
319 of location within the element, a marked improvement over CAM-SE. Since the state is approxi-
320 mately independent of in-element location, it follows that the physics forcing, which is evaluated
321 from the dynamical core state, may be expected to also show an improvement in grid-imprinting.

322 The low-level, mean and variance of the temperature tendencies from the physics in the two sim-
323 ulations are shown in Figure 9. The mean states in the two models resemble one another, consistent
324 with the zonal mean precipitaiton rates (Figure 8). The mean physics tendencies contains modest
325 grid imprinting in CAM-SE (barely visible near the storm-track regions), while in the variance
326 field, grid imprinting is both ubiquitous and unmistakable. The variance is larger on boundary
327 nodes, manifesting as a ‘stitching’ pattern resembling the cube-sphere grid. In CAM-SE-CSLAM,
328 the grid imprinting is all but eliminated based on the mean and variance of the physics tendencies
329 (Figure 9), consistent with our expectation.

330 As stated in Section 3, the mapping of the state to the physics grid and the reverse interpolation
331 of physics tendencies to the GLL grid is not total energy conserving. CAM has a global energy
332 fixer (Williamson et al. 2015) which can be used to estimate the errors associated with the mapping
333 algorithms. To do so, it is presumed that there are no compensating mapping errors in going to
334 and from the physics and dynamics grids, and that CAM-SE-CSLAM and CAM-SE have the same
335 energy dissipation rates. Under these assumptions the spurious globally integrated total energy
336 errors due to the mapping algorithm is estimated to be approximately 0.0025 W/m^2 in the aqua-

337 planet simulations. In comparison, the dynamical core total energy dissipation is on the order of
338 0.1 W/m^2 (Lauritzen et al. 2018).

339 *c. Held-Suarez with Topography*

340 Grid imprinting associated with the flow around obstacles is more problematic than that en-
341 countered on the aqua-planets. In order to diagnose grid imprinting due to topographic flow, an
342 idealized held-Suarez configuration (Held and Suarez 1994) is outfitted with real world topogra-
343 phy after Fox-Rabinovitz et al. (2000); Baer et al. (2006), and run for two years. Figure 10 shows
344 the mean ω at two different vertical levels in the middle troposphere. **The data are presented as a**
345 **raster plot on their respective unstructured grids, in order to delineate whether a particular value is**
346 **associated with an interior, edge or element boundary node.**

347 At higher latitudes (e.g., the southern Andes), the flow is smooth, conforming reasonably to the
348 underlying topography. At lower latitudes (within 20 to 30 degrees from the equator), over the
349 Andes or the Himalayas, there is a clear preference for extrema to occur at the element bound-
350 aries (Figure 10). The vertical structure of ω in regions of strong grid-imprinting indicates full-
351 troposphere upward/downward motion (not shown). Grid imprinting is therefore more common
352 in regions of weak stratification, such as occurs in the deep tropics, with forced up-slope flow
353 facilitating the release of gravitational instability. Resolved updrafts/downdrafts often align with
354 the element boundaries due to its systematically tighter pressure gradients.

355 Through the use of the quasi-equal area physics grid, grid imprinting due to topographic flow is
356 reduced (Figures 10). Figure 10 also shows the state in CAM-SE-CSLAM, but on the GLL grid.
357 Arguably, grid imprinting due to topography in CAM-SE-CSLAM is not much of an improvement
358 over CAM-SE, viewed from the GLL grid. The native topography lives on the physics grid, and the
359 topography is mapped to the nodal points at run-time in CAM-SE-CSLAM. Mapping topography

360 to the quadrature nodes ensures that no new extrema will be introduced to the boundary nodes,
361 where the solution is least smooth. This effect can not be very large, since the grid noise is similar
362 in CAM-SE and CAM-SE-CSLAM on the GLL grid. From the perspective of the physics grid,
363 the CAM-SE-CSLAM solution clearly mitigates the influence of grid-induced extrema on the state
364 (Figure 10). The reduction in grid imprinting in CAM-SE-CSLAM is therefore almost entirely a
365 result of the smoothing effect of integrating the basis functions over the control volumes of the
366 physics grid.

367 *d. AMIP type simulations*

368 A pair of 20 year-long AMIP type simulations are performed, using CAM, version 6 physics
369 package (CAM6) and using perpetual year 2000 SST boundary conditions (*F2000climo* compset
370 in CESM2.0; <https://doi.org/10.5065/D67H1H0V>). Figure 11 shows the climatological pre-
371 cipitation fields in CAM-SE (left) and CAM-SE-CSLAM (middle), and over the same mountain-
372 ous regions as in Figure 10. The plots have some similar features to the ω field in the Held-Suarez
373 runs; the greater variance at lower latitudes, and on the windward side of the mountains are broadly
374 similar. CAM-SE-CSLAM has a lower spatial variance, e.g., the lack of extrema over the Andes
375 at about 15° S compared to CAM-SE, and the grid-scale precipitation peak over the Himalayas
376 at about 30° N. The difference plot (Figure 11; right panel) is more broadly populated by blue,
377 purple and white contours, indicating that CAM-SE has, in general, lower magnitude precipitation
378 rates over high topography. The difference plots also highlight a couple of zonally aligned strips
379 of anomalous precipitation, in particular, near the foot of the Himalayas in CAM-SE. These bands
380 are in the same location as the bands of precipitation identified in CAM-SE in Lauritzen et al.
381 (2015a) (their Figure 7), but using CAM, version 5 physics, of which they argue are spurious in
382 nature.

383 To assist in identifying whether a particular precipitation pattern is spurious, an AMIP type sim-
384 ulation is carried out using the finite-volume dynamical core that uses a regular latitude-longitude
385 1° grid (CAM-FV; Neale et al. 2012). CAM-FV is the default low resolution model in CESM2.0,
386 and with its smoothly varying grid, does not suffer from the Quadrature Node Problem. Figure 12
387 shows the global precipitation fields in CAM-SE, CAM-SE-CSLAM and CAM-FV, compared to
388 an observational dataset, the GPCP (1979-2003) gridded dataset (Huffman et al. 2001). The mag-
389 nitude of the precipitation rates in all three models are higher than the GPCP dataset (note the
390 lack of red contours in the GPCP dataset), which should be interpreted cautiously due to widely-
391 accepted issues in constructing a reliable, gridded, global precipitation dataset. At lower latitudes,
392 CAM-FV has lower spatial variance, and overall lower magnitudes, compared with CAM-SE. The
393 GPCP dataset and CAM-FV together indicate that perhaps the precipitation rates in CAM-SE are
394 larger than in reality. Following suit, the reduction in magnitude and spatial variance in precipita-
395 tion in CAM-SE-CSLAM may be interpreted as an improvement over CAM-SE.

396 5. Conclusions

397 Element-based high-order Galerkin Methods possess many of the attractive qualities recom-
398 mended for next generation global atmospheric models. Among these, high-order accuracy is
399 achieved with minimal communication between elements, allowing for near perfect scaling on
400 massively parallel systems. Element communication amounts to a numerical flux applied to the
401 element boundaries, reconciling overlapping solutions of adjacent elements but degrading the
402 smoothness of the boundary nodes in the process (to C^0). For non-smooth problems, gradients are
403 systematically tighter at the element boundaries, and local extrema often characterize the boundary
404 nodes. This behavior is illustrated using NCAR's Community Atmosphere Model with Spectral

405 Elements dynamics (CAM-SE) in an aqua-planet configuration, in a Held-Suarez configuration
406 with real-world topography **and in an AMIP type configuration.**

407 The authors argue that the conventional physics-dynamics coupling paradigm, in which the
408 physical parameterizations are evaluated on the dynamical core grid, exacerbates grid imprinting.

409 A separate physics grid is proposed and implemented in CAM-SE, and referred to as CAM-SE-
410 CSLAM, through dividing the elements into quasi-equal areas with equivalent degrees of freedom.

411 The state is mapped to the physics grid with high-order accuracy through integrating CAM-SE's
412 Lagrange basis functions over the control volumes. Control volumes near element boundaries now

413 represent a state in the vicinity of the extrema produced through the boundary exchange, as op-
414 posed to the the nodal value itself. These control volumes are also compatible with a 'large-scale

415 state' as required by the physical parameterizations. The physical parameterizations are evalu-
416 ated on the finite volume grid, and the forcing terms are mapped back to the dynamical core grid

417 using a cubic tensor-product Lagrange interpolation. In aqua-planet simulations, evaluating the
418 parameterizations on the physics grid removes any obvious dependence of proximity to the ele-

419 ment boundary, resulting in a more realistic state with negligible grid imprinting. The mapping
420 algorithm does not conserve total energy, but it is estimated that these errors are one to two orders
421 of magnitude less than the total energy dissipation from the dynamical core.

422 In CAM-SE-CSLAM, the physics grid replaces the default CAM-SE quadrature point-based
423 coupler grid (Figure 4) to compute fluxes between model components in the Community Earth

424 System Model (CESM). The appeal here is two-fold. Through integrating the Lagrange basis
425 functions over control volumes, one can be certain that the fluxes computed from this grid are
426 a volume averaged flux. The same can not be said for CAM-SE, where the nodal values are

427 effectively assigned to each control volume. The second advantage of the new coupler grid is
428 that extrema occurring on boundary nodes may no longer influence other model components, in

429 simulations without rough topography. While grid imprinting is effectively eliminated in the aqua-
430 planets, experiments with real-world topography (Held-Suarez and AMIP type configurations)
431 reduces, but does not entirely eliminate, imprinting from the mean state. The quasi-equal area
432 physics grid is nonetheless effective at mitigating numerical nuances associated with high-order
433 element-based Galerkin methods, for non-smooth problems.

434 *Acknowledgments.* NCAR is sponsored by the National Science Foundation (NSF). We thank
435 three anonymous reviewers for their helpful comments that significantly improved the clarity of
436 the manuscript. Herrington thanks NCAR’s Computational and Information Systems Laboratory
437 (CISL) and NCAR’s Climate and Global Dynamics division (CGD) for computational resources
438 and technical support. Herrington, Reed, and Lauritzen are grateful to the NCAR Advanced Study
439 Program graduate visitor program for funding Herrington’s 12-month visit. Goldhaber was par-
440 tially supported by the Accelerated Climate Modeling for Energy (ACME) project, and work pack-
441 age 12 – 015334 “Multiscale Methods for Accurate, Efficient, and the Accelerated Scale-Aware
442 Models, both funded through the U.S. Department of Energy Office of Biological and Environ-
443 mental Resarch. Goldhaber is also partially supported through NSF award AGS-1500187 “De-
444 velopment and Testing of a Global Quasi 3-D multi Modeling Framework.” Model source code is
445 officially released with CESM2.1 (<https://doi.org/10.5065/D67H1H0V>).

446 APPENDIX

447 The mapping of the physics tendencies from the physics grid to the GLL grid is done with
448 tensor-cubic Lagrange interpolation. The elements of the cubed-sphere in SE are created
449 from an equi-angular gnomonic projection. Consider one element $(\alpha, \beta) \in [\alpha_1^{(elem)}, \alpha_2^{(elem)}] \times$
450 $[\beta_1^{(elem)}, \beta_2^{(elem)}]$, where (α, β) are central angle coordinates and $\alpha_1^{(elem)}$ and $\alpha_2^{(elem)}$ are the min-
451 imum and maximum central angles in the α -coordinate direction, respectively, and similarly for

⁴⁵² β . Let $\Delta\alpha^{(elem)} = \alpha_2^{(elem)} - \alpha_1^{(elem)}$ and $\Delta\beta^{(elem)} = \beta_2^{(elem)} - \beta_1^{(elem)}$. The physics grid cell central
⁴⁵³ angle centers are located at

$$(\alpha_i^{(pg)}, \beta_j^{(pg)}) = \left[\alpha_1^{(elem)} + (i - \frac{1}{2}) \Delta\alpha^{(pg)}, \right. \\ \left. \beta_1^{(elem)} + (j - \frac{1}{2}) \Delta\beta^{(pg)} \right], \quad (\text{A1})$$

⁴⁵⁴ where $\Delta\alpha^{(pg)} = \Delta\beta^{(pg)} = \frac{\Delta\alpha^{(elem)}}{pg} = \frac{\Delta\beta^{(elem)}}{pg}$. The interpolation is performed in central-angle co-
⁴⁵⁵ ordinates using tensor product cubic interpolation. For elements located on a cubed-sphere edge
⁴⁵⁶ or corner the coordinate system for neighboring elements may be on a different panel. To take
⁴⁵⁷ into account this coordinate change the central angle locations of physics grid cell centers located
⁴⁵⁸ on other panels are transformed to the coordinate system of the panel the element in question is
⁴⁵⁹ located on (the transformations are given in, e.g., Nair et al. 2005). An illustration is given in
⁴⁶⁰ Figure 13 for an element located in the lower left corner of a panel. The element in question is
⁴⁶¹ $(\xi, \chi) \in (-1, 1)^2$ where, for simplicity, we have transformed the element coordinates into normal-
⁴⁶² ized coordinates $(\xi, \chi) = \left(\frac{2(\alpha^{(pg)} - \alpha_1^{(elem)})}{\Delta\alpha^{(elem)}} - 1, \frac{2(\beta^{(pg)} - \beta_1^{(elem)})}{\Delta\beta^{(elem)}} - 1 \right)$; also used internally in the
⁴⁶³ SE dynamical core (see, e.g., section 3.3 in Lauritzen et al. 2018). The GLL points are located at
⁴⁶⁴ $-1, -\sqrt{5}/5, \sqrt{5}/5$, and 1 in each coordinate direction. Near the edges/corners of an element cubic
⁴⁶⁵ extrapolation is used if the centered stencil expands beyond the panel.

⁴⁶⁶ References

- ⁴⁶⁷ Arakawa, A., and W. H. Schubert, 1974: Interaction of a cumulus cloud ensemble with the large-
⁴⁶⁸ scale environment, Part I. *J. Atmos. Sci.*, **31**, 674–701.
- ⁴⁶⁹ Bacmeister, J. T., K. A. Reed, C. Hannay, P. Lawrence, S. Bates, J. E. Truesdale, N. Rosen-
⁴⁷⁰ bloom, and M. Levy, 2018: Projected changes in tropical cyclone activity under future warm-

- 471 ing scenarios using a high-resolution climate model. *Climatic Change*, **146**, 547–560, doi:
472 10.1007/s10584-016-1750-x, URL <http://dx.doi.org/10.1007/s10584-016-1750-x>.
- 473 Baer, F., H. Wang, J. J. Tribbia, and A. Fournier, 2006: Climate modeling with spectral elements.
474 *Mon. Wea. Rev.*, **134**, 3610–3624, doi:10.1175/MWR3360.1, URL <http://dx.doi.org/10.1175/MWR3360.1>.
- 475 Brdar, S., M. Baldauf, A. Dedner, and R. Klöfkorn, 2013: Comparison of dynamical cores for
476 nwp models: comparison of cosmo and dune. *Theoretical and Computational Fluid Dynamics*,
477 **27** (3-4), 453–472, doi:10.1007/s00162-012-0264-z.
- 478 Canuto, C., M. Y. Hussaini, A. Quarteroni, and T. Zang, 2007: *Spectral Methods: Evolution to
479 Complex Geometries and Applications to Fluid Dynamics*. 1st ed., Springer.
- 480 Dennis, J. M., and Coauthors, 2012: CAM-SE: A scalable spectral element dynamical core for
481 the Community Atmosphere Model. *Int. J. High. Perform. C.*, **26** (1), 74–89, doi:10.1177/
482 1094342011428142, URL <http://hpc.sagepub.com/content/26/1/74.abstract>, <http://hpc.sagepub.com/content/26/1/74.full.pdf+html>.
- 483 Durran, D., 2010: *Numerical Methods for Fluid Dynamics: With Applications to Geophysics*,
484 Texts in Applied Mathematics, Vol. 32. 2nd ed., Springer, 516 p.
- 485 Fournier, A., M. A. Taylor, and J. J. Tribbia, 2004: The spectral element atmosphere model
486 (SEAM): High-resolution parallel computation and localized resolution of regional dynamics.
487 *Mon. Wea. Rev.*, **132** (3), 726–748.
- 488 Fox-Rabinovitz, M. S., G. L. Stenchikov, M. J. Suarez, L. L. Takacs, and R. C. Govindaraju, 2000:
489 A uniform- and variable-resolution stretched-grid gcm dynamical core with realistic orography.
490 *Mon. Wea. Rev.*, **128**, 1883–1898.

- 493 Giraldo, F., and M. Restelli, 2008: A study of spectral element and discontinuous galerkin methods
494 for the Navier-Stokes equations in nonhydrostatic mesoscale atmospheric modeling: Equation
495 sets and test cases. *J. Comput. Phys.*, **227** (8), 3849 – 3877, doi:<http://dx.doi.org/10.1016/j.jcp>.
496 2007.12.009.
- 497 Guba, O., M. Taylor, and A. St-Cyr, 2014a: Optimization-based limiters for the spectral element
498 method. *J. Comput. Phys.*, **267** (0), 176 – 195, doi:<http://dx.doi.org/10.1016/j.jcp.2014.02.029>.
- 499 Guba, O., M. A. Taylor, P. A. Ullrich, J. R. Overfelt, and M. N. Levy, 2014b: The spectral element
500 method (sem) on variable-resolution grids: evaluating grid sensitivity and resolution-aware nu-
501 matical viscosity. *Geosci. Model Dev.*, **7** (6), 2803–2816, doi:[10.5194/gmd-7-2803-2014](https://doi.org/10.5194/gmd-7-2803-2014).
- 502 Held, I. M., and M. J. Suarez, 1994: A proposal for the intercomparison of the dynamical cores of
503 atmospheric general circulation models. *Bull. Am. Meteorol. Soc.*, **73**, 1825–1830.
- 504 Huffman, G. J., R. F. Adler, M. M. Morrissey, D. T. Bolvin, S. Curtis, R. Joyce, B. McGavock,
505 and J. Susskind, 2001: Global precipitation at one-degree daily resolution from multisatellite
506 observations. *J. Hydrometeorology*, **2** (1), 36–50.
- 507 Kessler, E., 1969: On the distribution and continuity of water substance in atmospheric circula-
508 tions. *Meteorol. Monogr.*, **10** (32), 88.
- 509 Kim, Y.-J., F. X. Giraldo, M. Flatau, C.-S. Liou, and M. S. Peng, 2008: A sensitivity study of the
510 kelvin wave and the Madden-Julian oscillation in aquaplanet simulations by the Naval Research
511 Laboratory Spectral Element Atmospheric Model. *J. Geo. Res.: Atmospheres*, **113** (D20), doi:
512 [10.1029/2008JD009887](https://doi.org/10.1029/2008JD009887), d20102.

- 513 Lauritzen, P. H., J. T. Bacmeister, P. F. Callaghan, and M. A. Taylor, 2015a: Ncar global model
514 topography generation software for unstructured grids. *Geoscientific Model Development Discussions*, **8** (6), 4623–4651, doi:10.5194/gmdd-8-4623-2015.
- 515
- 516 Lauritzen, P. H., A. J. Conley, J.-F. Lamarque, F. Vitt, and M. A. Taylor, 2015b: The terminator
517 “toy” chemistry test: a simple tool to assess errors in transport schemes. *Geoscientific Model
518 Development*, **8** (5), 1299–1313, doi:10.5194/gmd-8-1299-2015.
- 519 Lauritzen, P. H., M. A. Taylor, J. Overfelt, P. A. Ullrich, R. D. Nair, S. Goldhaber, and
520 R. Kelly, 2017: CAM-SE-CSLAM: Consistent coupling of a conservative semi-lagrangian
521 finite-volume method with spectral element dynamics. *Mon. Wea. Rev.*, **145** (3), 833–855, doi:
522 10.1175/MWR-D-16-0258.1.
- 523 Lauritzen, P. H., and Coauthors, 2018: Ncar cesm2.0 release of cam-se: A reformulation of the
524 spectral-element dynamical core in dry-mass vertical coordinates with comprehensive treatment
525 of condensates and energy. *J. Adv. Model. Earth Syst.*, doi:10.1029/2017MS001257.
- 526 Lin, S.-J., 2004: A ‘vertically Lagrangian’ finite-volume dynamical core for global models. *Mon.
527 Wea. Rev.*, **132**, 2293–2307.
- 528 Maday, Y., and A. T. Patera, 1987: Spectral element methods for the incompressible Navier Stokes
529 equations. *State of the Art Surveys on Computational Mechanics*, A. K. Noor, and J. T. Oden,
530 Eds., ASME, New York, 71–143.
- 531 Medeiros, B., D. L. Williamson, and J. G. Olson, 2016: Reference aquaplanet climate in the
532 community atmosphere model, version 5. *J. Adv. Model. Earth Syst.*, **8** (1), 406–424, doi:10.
533 1002/2015MS000593.

- 534 Nair, R., H.-W. Choi, and H. Tufo, 2009: Computational aspects of a scalable high-order dis-
535 continuous galerkin atmospheric dynamical core. *Computers & Fluids*, **38** (2), 309 – 319, doi:
536 <http://dx.doi.org/10.1016/j.compfluid.2008.04.006>.
- 537 Nair, R. D., M. N. Levy, and P. H. Lauritzen, 2011: Emerging numerical methods for atmo-
538 spheric modeling, in: P.H. Lauritzen, R.D. Nair, C. Jablonowski, M. Taylor (Eds.), Numerical
539 techniques for global atmospheric models. *Lecture Notes in Computational Science and Engi-
540 neering, Springer*, **80**.
- 541 Nair, R. D., S. J. Thomas, and R. D. Loft, 2005: A discontinuous galerkin transport scheme on the
542 cubed sphere. *Mon. Wea. Rev.*, **133** (4), 814–828, doi:10.1175/MWR2890.1.
- 543 Neale, R. B., and B. J. Hoskins, 2000: A standard test for agcms including their physical
544 parametrizations: I: the proposal. *Atmos. Sci. Lett.*, **1** (2), 101–107, doi:10.1006/asle.2000.0022.
- 545 Neale, R. B., and Coauthors, 2010: Description of the NCAR Community Atmosphere Model
546 (CAM 4.0). NCAR Technical Note, National Center of Atmospheric Research.
- 547 Neale, R. B., and Coauthors, 2012: Description of the NCAR Community Atmosphere Model
548 (CAM 5.0). NCAR Technical Note NCAR/TN-486+STR, National Center of Atmospheric Re-
549 search.
- 550 Plant, G. C. C., R. S., 2008: A stochastic parameterization for deep convection based on equilib-
551 rium statistics. *J. Atmos. Sci.*, **65**, 87–105, doi:10.1175/2007JAS2263.1, URL <http://dx.doi.org/10.1175/2007JAS2263.1>.
- 553 Polvani, L., A. Clement, B. Medeiros, J. Benedict, and I. Simpson, 2017: Opening the door to
554 simpler climate models in the community earth system model project. *EOS*, submitted.

- 555 Putman, W. M., and S.-J. Lin, 2007: Finite-volume transport on various cubed-sphere grids. *J.*
556 *Comput. Phys.*, **227** (1), 55–78.
- 557 Reed, K. A., J. T. Bacmeister, N. A. Rosenbloom, M. F. Wehner, S. C. Bates, P. H. Lauritzen,
558 J. E. Truesdale, and C. Hannay, 2015: Impact of the dynamical core on the direct simulation
559 of tropical cyclones in a high-resolution global model. *Geophys. Res. Lett.*, **42** (9), 3603–3608,
560 doi:10.1002/2015GL063974.
- 561 Rhoades, A. M., X. Huang, P. A. Ullrich, and C. M. Zarzycki, 2016: Characterizing sierra
562 nevada snowpack using variable-resolution cesm. *Journal of Applied Meteorology and Cli-*
563 *matology*, **55** (1), 173–196, doi:10.1175/JAMC-D-15-0156.1, URL <https://doi.org/10.1175/JAMC-D-15-0156.1>.
- 564
- 565 Simmons, A. J., and D. M. Burridge, 1981: An energy and angular-momentum conserving vertical
566 finite-difference scheme and hybrid vertical coordinates. *Mon. Wea. Rev.*, **109** (4), 758–766.
- 567 Small, R. J., and Coauthors, 2014: A new synoptic scale resolving global climate simulation using
568 the community earth system model. *Journal of Advances in Modeling Earth Systems*, **6** (4),
569 1065–1094, doi:10.1002/2014MS000363.
- 570 Suarez, M. J., A. Arakawa, and D. A. Randall, 1983: The parameterization of the planetary
571 boundary layer in the ucla general circulation model: Formulation and results. *Mon. Wea. Rev.*,
572 **111** (11), 2224–2243.
- 573 Taylor, M., J. Edwards, and A. St-Cyr, 2008: Petascale atmospheric models for the community
574 climate system model: new developments and evaluation of scalable dynamical cores. *J. Phys.:
575 Conf. Ser.*, **125**, doi:10.1088/1742-6596/125/1/012023.

- 576 Taylor, M. A., and A. Fournier, 2010: A compatible and conservative spectral element method on
577 unstructured grids. *J. Comput. Phys.*, **229** (17), 5879 – 5895, doi:10.1016/j.jcp.2010.04.008.
- 578 Thatcher, D. R., and C. Jablonowski, 2016: A moist aquaplanet variant of the Held–Suarez test
579 for atmospheric model dynamical cores. *Geoscientific Model Development*, **9** (4), 1263–1292,
580 doi:10.5194/gmd-9-1263-2016, URL <https://www.geosci-model-dev.net/9/1263/2016/>.
- 581 Ullrich, P. A., 2014: A global finite-element shallow-water model supporting continuous and dis-
582 continuous elements. *Geosci. Model Dev.*, **7** (6), 3017–3035, doi:10.5194/gmd-7-3017-2014.
- 583 Ullrich, P. A., D. Devendran, and H. Johansen, 2016: Arbitrary-order conservative and consistent
584 remapping and a theory of linear maps: Part ii. *Mon. Wea. Rev.*, **144** (4), 1529–1549, doi:
585 10.1175/MWR-D-15-0301.1.
- 586 Ullrich, P. A., T. Melvin, C. Jablonowski, and A. Staniforth, 2014: A proposed baroclinic wave test
587 case for deep and shallow-atmosphere dynamical cores. *Quart. J. Royal Meteor. Soc.*, **140** (682),
588 1590–1602.
- 589 Ullrich, P. A., and M. A. Taylor, 2015: Arbitrary-order conservative and consistent remap-
590 ping and a theory of linear maps: Part I. *Mon. Wea. Rev.*, **143**, 2419–2440, doi:10.1175/
591 MWR-D-14-00343.1.
- 592 Ullrich, P. A., and Coauthors, 2017: Dcmip2016: A review of non-hydrostatic dynamical core
593 design and intercomparison of participating models. *Geosci. Model Dev.*, **10**, 4477–4509, doi:
594 10.5194/gmd-10-4477-2017.
- 595 Wan, H., and Coauthors, 2013: The icon-1.2 hydrostatic atmospheric dynamical core on triangular
596 grids, part i: formulation and performance of the baseline version. *Geosci. Model Dev.*, **6**, 735–
597 763.

- 598 Williamson, D. L., 2002: Time-split versus process-split coupling of parameterizations and dy-
599 namical core. *Mon. Wea. Rev.*, **130**, 2024–2041.
- 600 Williamson, D. L., J. G. Olson, C. Hannay, T. Toniazzo, M. Taylor, and V. Yudin, 2015: Energy
601 considerations in the community atmosphere model (cam). *J. Adv. Model. Earth Syst.*, **7** (3),
602 1178–1188, doi:10.1002/2015MS000448, URL <http://dx.doi.org/10.1002/2015MS000448>.
- 603 Zarzycki, C. M., C. Jablonowski, and M. A. Taylor, 2014a: Using variable-resolution meshes to
604 model tropical cyclones in the community atmosphere model. *Mon. Wea. Rev.*, **142** (3), 1221–
605 1239, doi:10.1175/MWR-D-13-00179.1.
- 606 Zarzycki, C. M., M. N. Levy, C. Jablonowski, J. R. Overfelt, M. A. Taylor, and P. A. Ullrich,
607 2014b: Aquaplanet experiments using cam’s variable-resolution dynamical core. *J. Climate*,
608 **27** (14), 5481–5503, doi:10.1175/JCLI-D-14-00004.1.
- 609 Zhang, K., and Coauthors, 2017: Impact of numerical choices on water conservation in the e3sm
610 atmosphere model version 1 (eam v1). *Geoscientific Model Development Discussions*, **2017**,
611 1–26, doi:10.5194/gmd-2017-293.

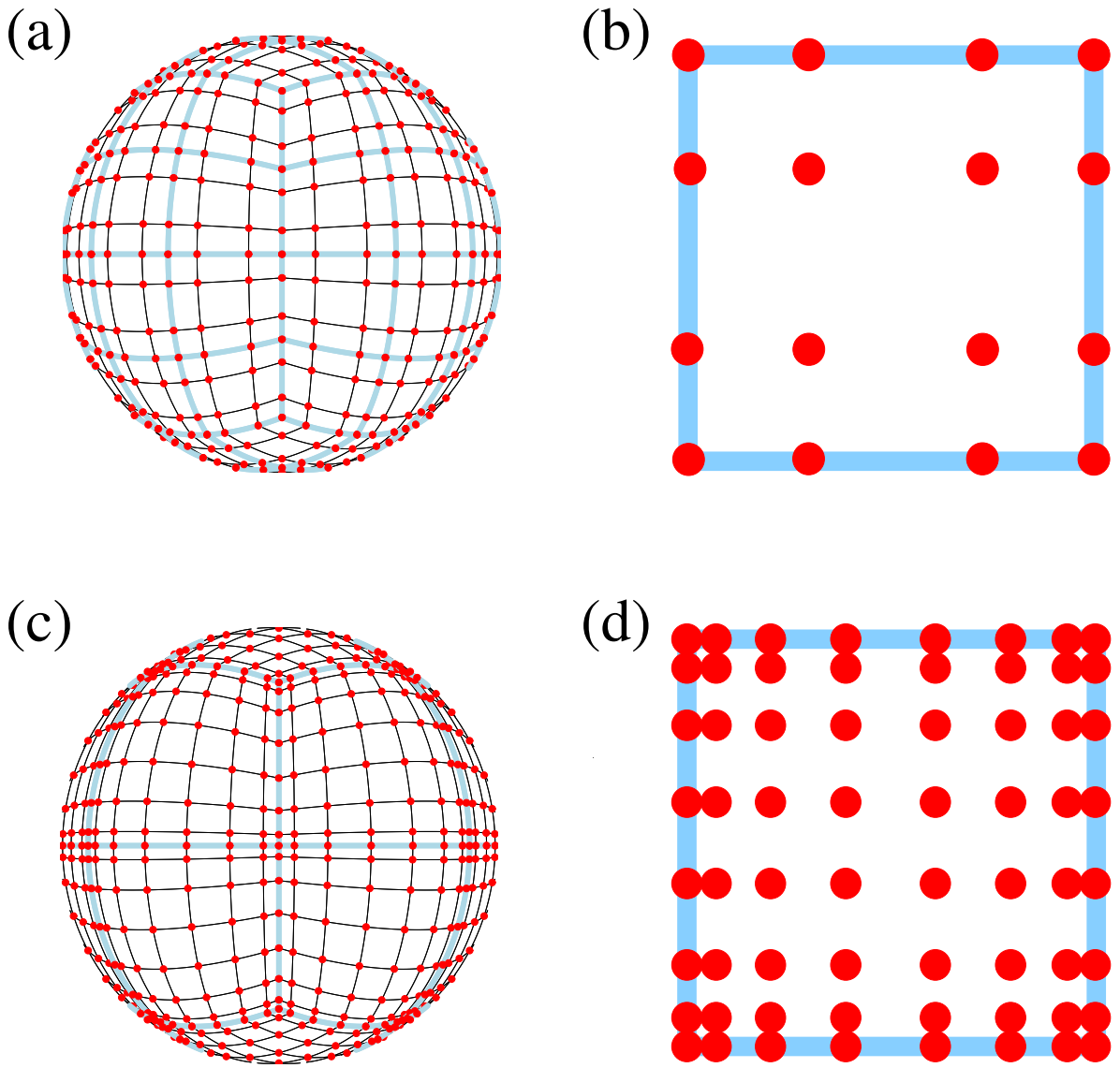
612 LIST OF FIGURES

- 655 **Fig. 10.** Mean ω at two model levels in the middle troposphere, in a Held-Suarez configuration
 656 outfitted with real world topography. (Left) CAM-SE state on the GLL grid, *ne30np4*,
 657 (Middle) CAM-SE-CSLAM state on the GLL grid, *ne30np4* and (Right) CAM-SE-CSLAM
 658 state on the physics grid, *ne30pg3*. The ω fields are computed from a 1200 day Held-Suarez
 659 simulation. The data are contoured according to a ‘cell fill’ approach, in which the coupler
 660 grids (e.g., Figure 4) are used to delineate the vertices of the control volumes. 41

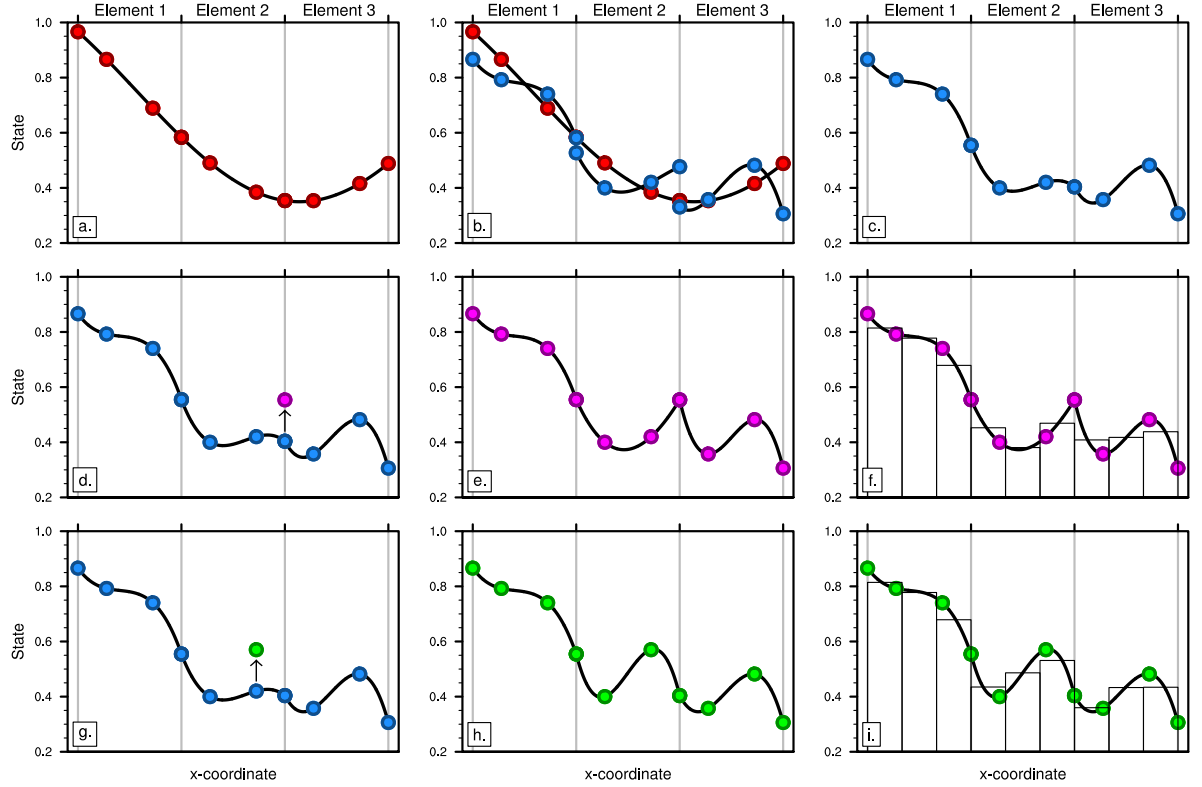
661 **Fig. 11.** Climatological total precipitation rate computed from the final 19 years of a pair of 20 year
 662 long AMIP type simulations. (Left) CAM-SE, (middle) CAM-SE-CSLAM and (Right) their
 663 differences. The difference field is computed through bilinearly interpolating to a common
 664 latitude-longitude grid. 42

665 **Fig. 12.** Climatological total precipitation rate computed from the final 19 years of a suite of 20
 666 year long AMIP simulations, using CAM-SE (*ne30np4*), CAM-SE-CSLAM (*ne30np3*) and
 667 CAM-FV (*f09*). The top plot is an observational product, the gridded GPCP climatological
 668 precipitation dataset. 43

669 **Fig. 13.** Schematic of the coordinate system in which the dimensionally split cubic Lagrange in-
 670 terpolation is computed. The physics grid centers are marked with asterisks and the GLL
 671 points, we are interpolating to, with solid filled circles. The element in which the GLL
 672 points are located is bounded by thick black lines and located in the lower left corner of a
 673 panel. The stippled lines mark the boundaries of the remaining elements. For simplicity we
 674 are using the normalized coordinate centered at the element on which the GLL points we
 675 are interpolating to are located. Note that the coordinates for points on neighboring panels
 676 (using a different local coordinate system) must be transformed to the coordinate system of
 677 the element in question. 44



678 FIG. 1. Example of CAM-SE GLL quadrature grids, marked with red filled circles, (a & c) on the cubed-
 679 sphere and (b & d) in an element. (a)-(b) and (c)-(d) use 4×4 ($np = 4$) and 8×8 ($np = 8$) GLL quadrature
 680 points in each element, respectively. (a) and (c) have the same average grid-spacing at the Equator (7.5°) which is
 681 obtained by using (a) 4×4 ($ne = 4$) and (b) 2×2 ($ne = 2$) elements on each cubed-sphere face/panel, respectively.
 682 The element boundaries are marked with thick light blue lines. The grid configurations shown on (a) and (c) are
 683 referred to as $ne4np4$ and $ne2np8$, respectively.



684 FIG. 2. A one-dimensional schematic showing the relationship between the basis functions, the quadrature
 685 nodes and the proposed physics grid, over the coarse of a time-step. The filled circles are the GLL quadrature
 686 points in each element, which are connected by a Lagrange polynomials basis (curves). (a) Smooth initial con-
 687 dition are (b) advanced by the dynamics one Runge-Kutta step (blue), and (c) shows the solution after applying
 688 the DSS operator. Applying (d) grid-scale forcing to an element boundary node, (e) the basis representation is
 689 clearly C^0 at the element boundary. In contrast, (d) applying grid-scale forcing to an interior node (e) results
 690 in a smooth, C^∞ continuous field. (f),(i) Vertical bars pertain to the values on the physics grid, found through
 691 integrating the basis functions over the control volumes.

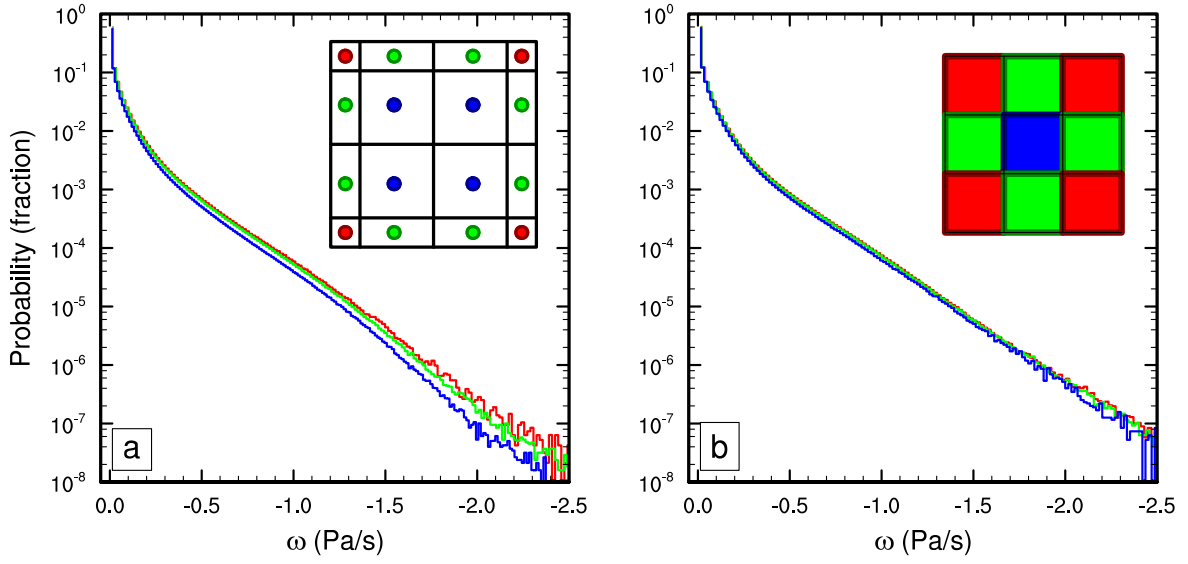
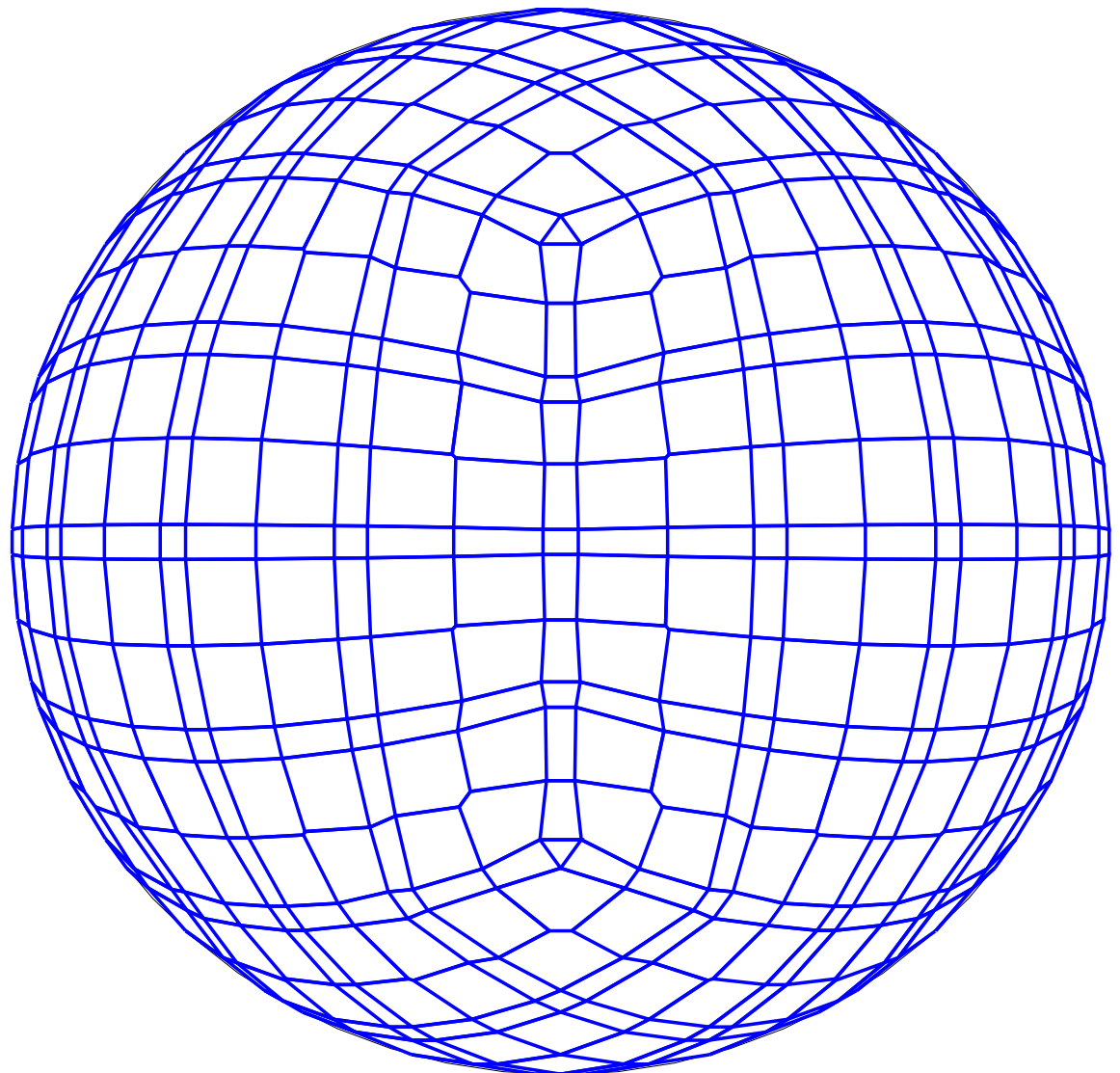
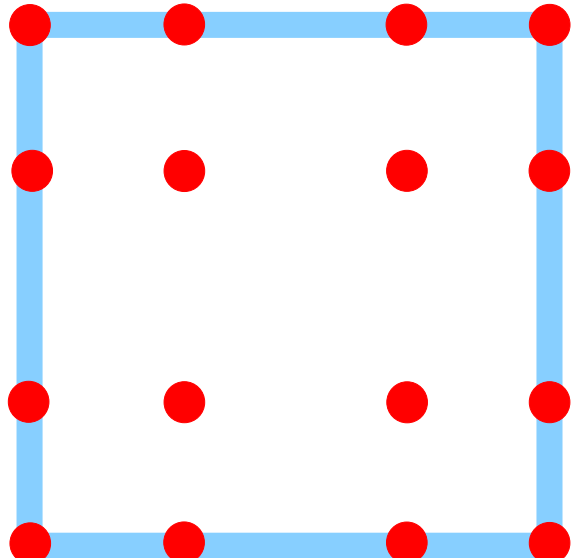


FIG. 3. Probability density distribution of instantaneous upward ω in a pair of aqua-planet simulations using CAM4 physics. Figure is constructed from one year of six hourly data, at all vertical levels. (a) *ne30np4* configuration conditionally sampled for interior, edge and corner node control volumes, and similarly (b) for the *ne30pg3* configuration. Note the consistently larger magnitude ω for boundary nodes compared with interior nodes in (a), and that the bias is substantially reduced through mapping to a quasi-equal area physics grid.

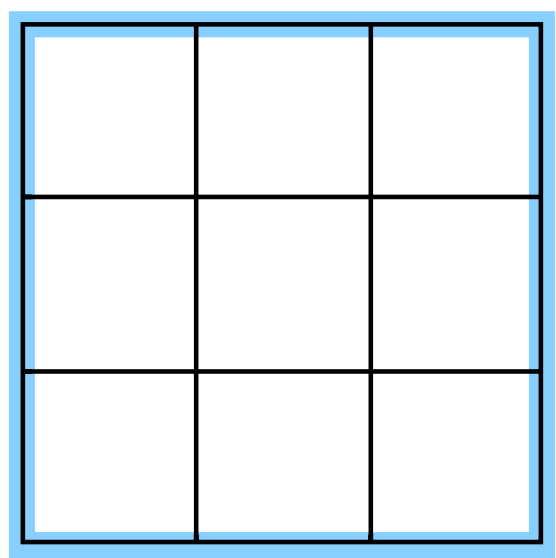


697 FIG. 4. An example of control volumes constructed around GLL quadrature points ($ne4np4$) so that the
698 spherical area of the control volumes exactly match the quadrature weight multiplied by the metric factor.

$$np = 4$$



$$pg = 3$$



699 FIG. 5. A schematic illustration of an element, indicating the relationship between (left) the dynamical core
700 grid, and (right) the proposed quasi-equal area physics grid. The physics grid contains $pg \times pg = 3 \times 3$ grid cells
701 in each element.

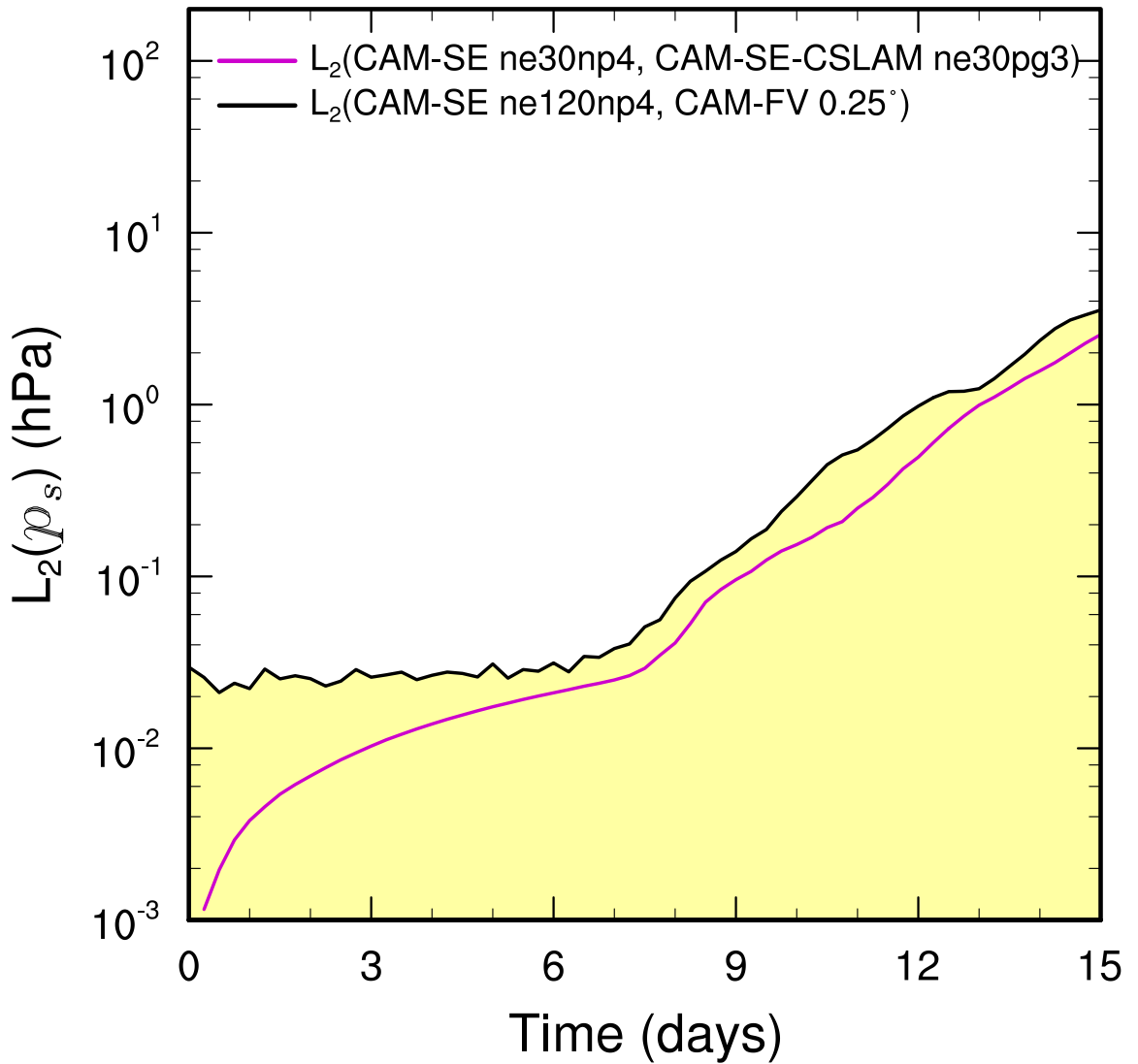
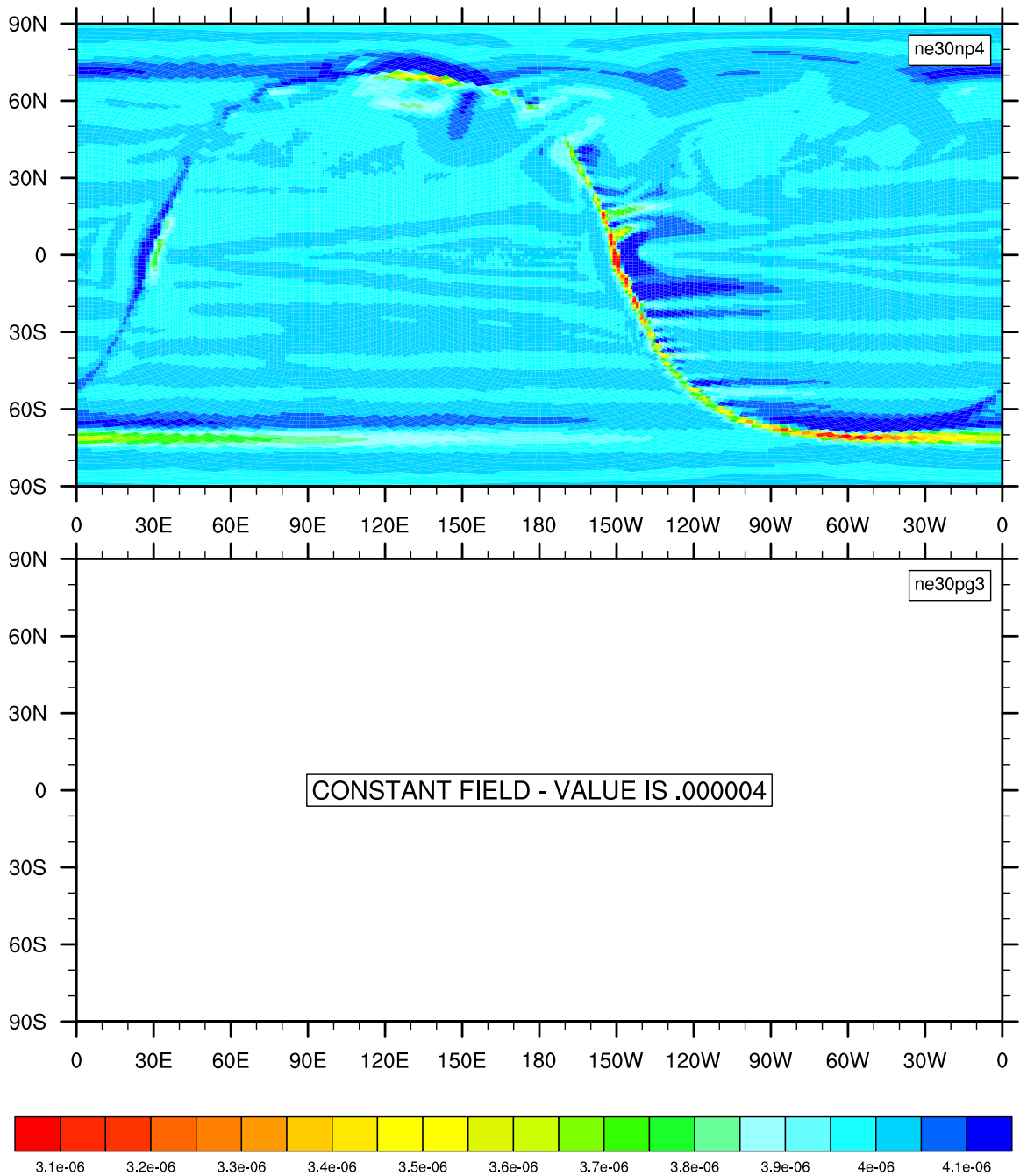
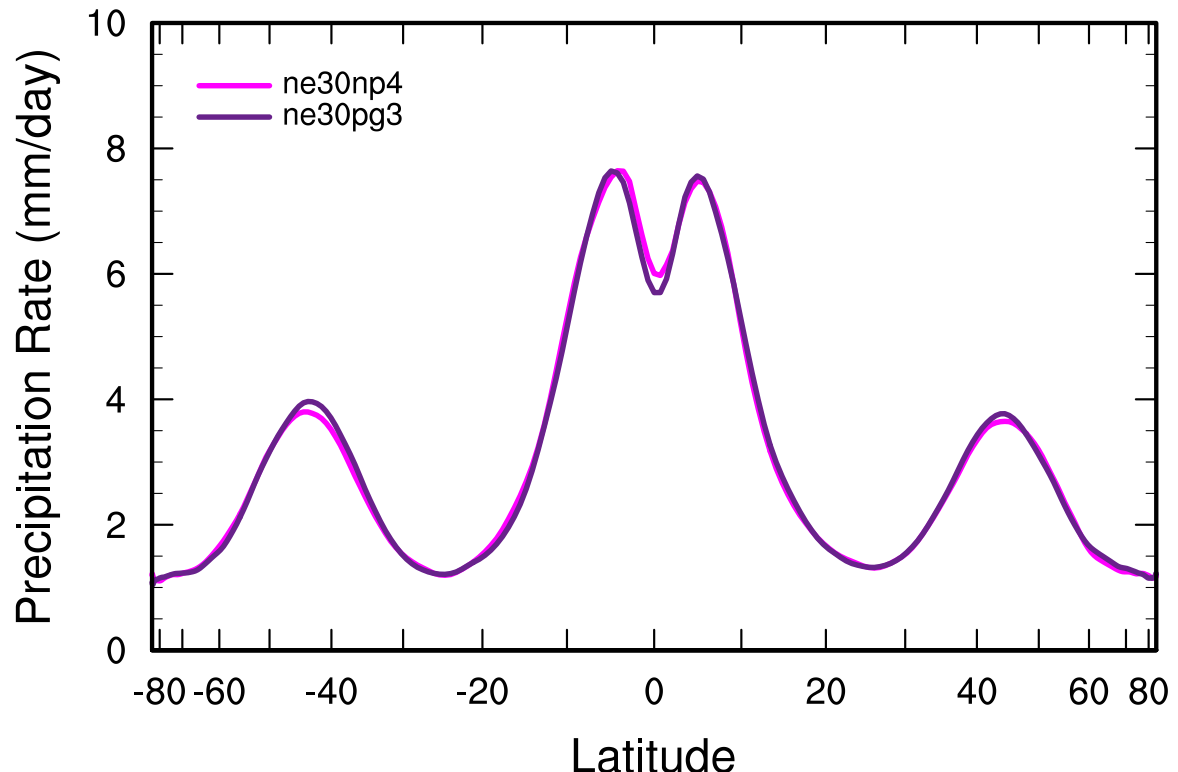


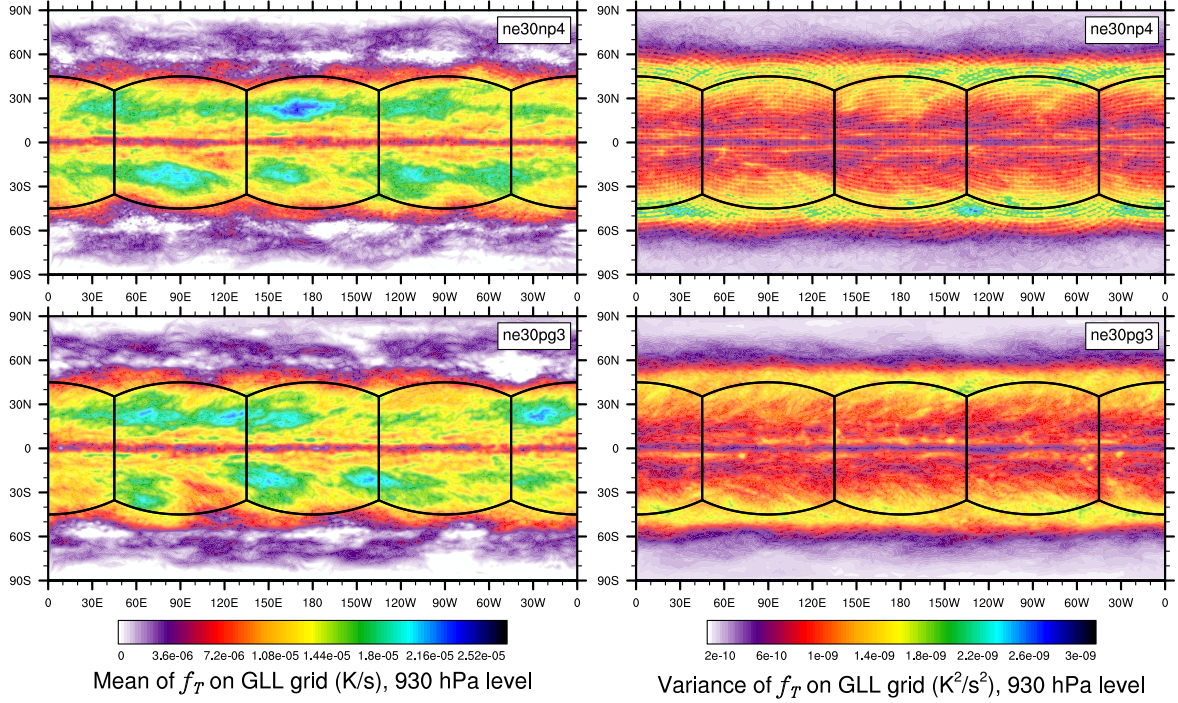
FIG. 6. L_2 difference norms of the surface pressure field, p_s , in the moist baroclinic wave simulations. L_2 values lying within the yellow region fall below the estimate of the uncertainty in the reference solution (black curve), computed as the difference norm between two approximately 0.25° resolution versions of CAM, the spectral-element and finite-volume (CAM-FV) dynamical cores.



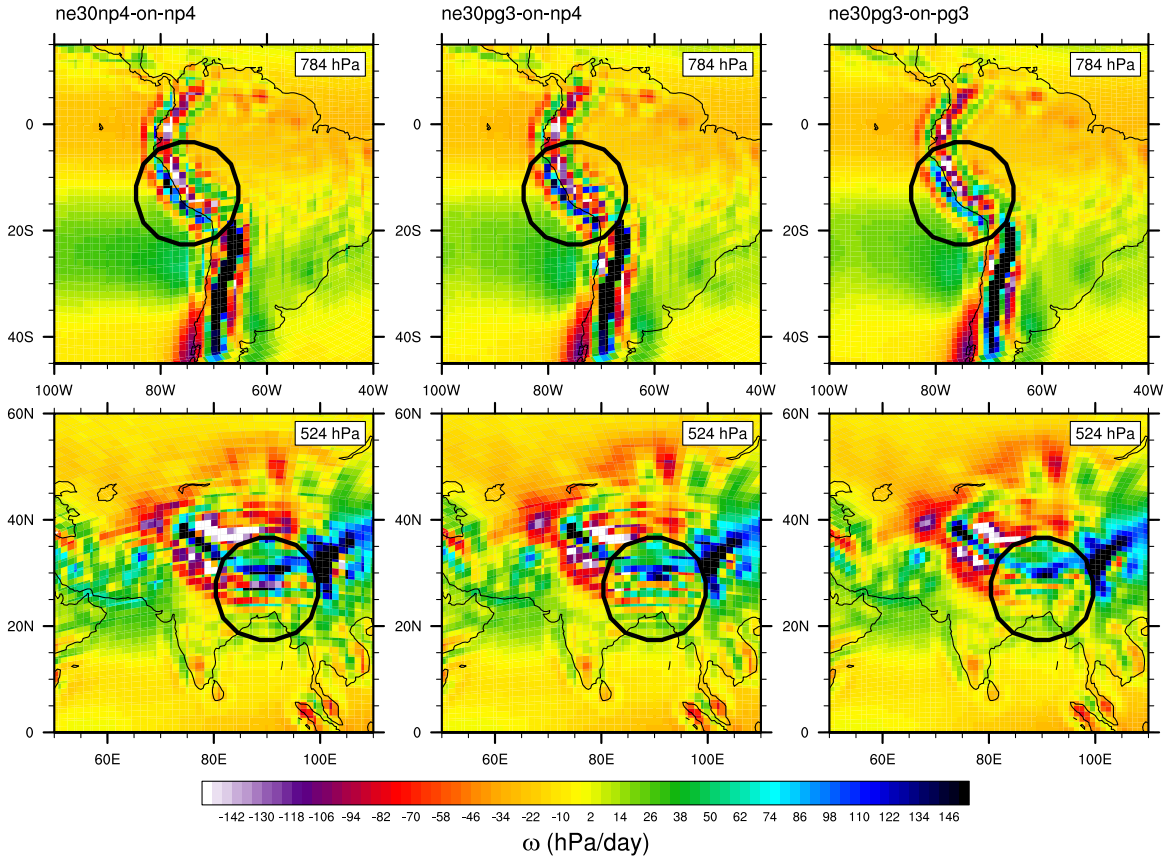
706 FIG. 7. Results of the terminator "toy"-chemistry test. Snapshot of the total column tracer mass at day 15 of
 707 the moist baroclinic wave test. (Top) CAM-SE, (Bottom) CAM-SE-CSLAM.



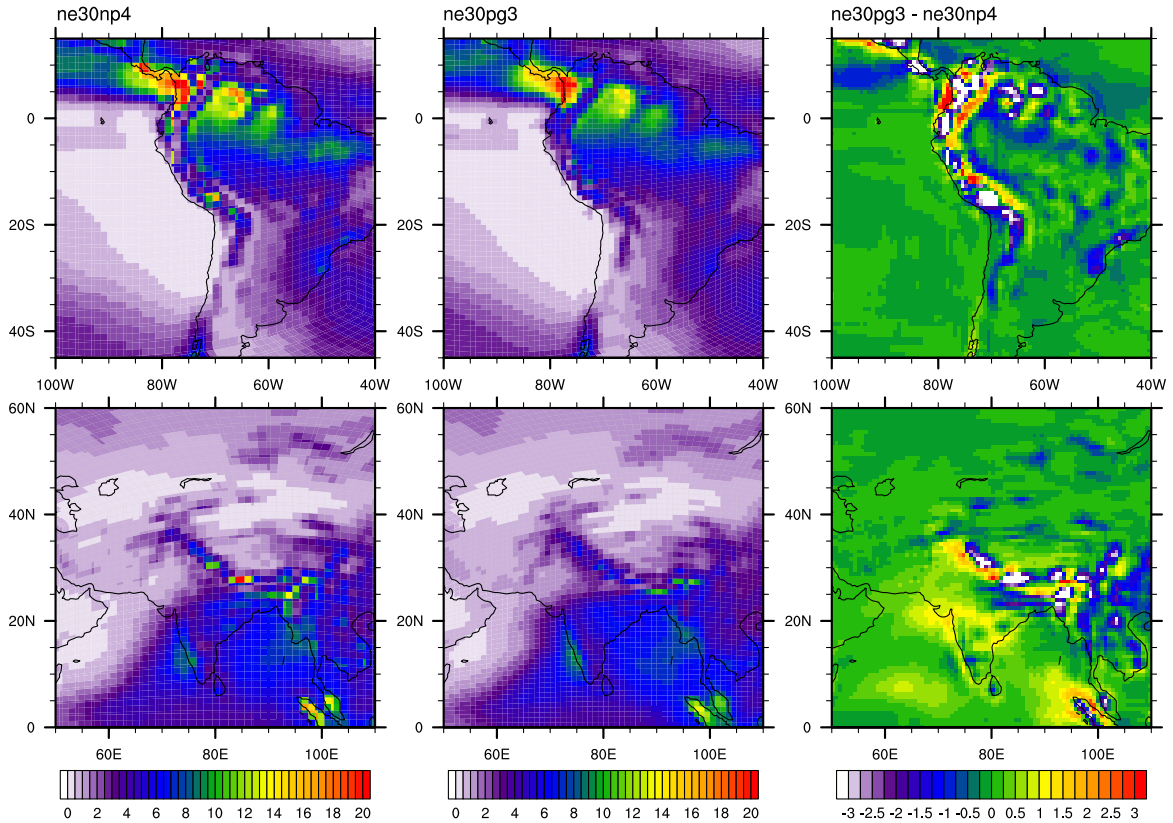
708 FIG. 8. Climatological zonal-mean total precipitation rate in the aqua-planets, computed from a pair of year
709 long simulations.



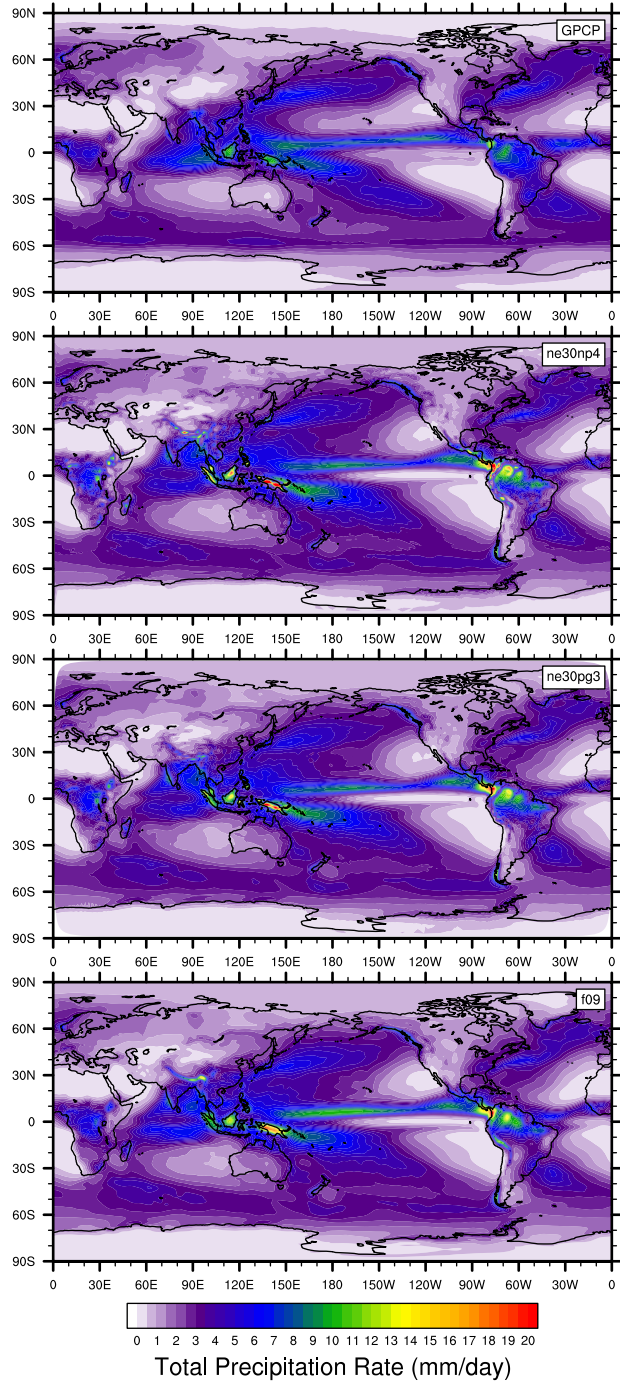
710 FIG. 9. Mean (left) and variance (right) of the low level temperature tendencies from the physical parameteri-
 711 zations on the GLL grid, with the ne30np4 configuration, (top row) and ne30pg3 configuration (bottom row), in
 712 a pair of year-long aqua-planet simulations after Medeiros et al. (2016). Grid imprinting is observed along the
 713 element boundaries in ne30np4, but is absent from the ne30pg3 simulation.



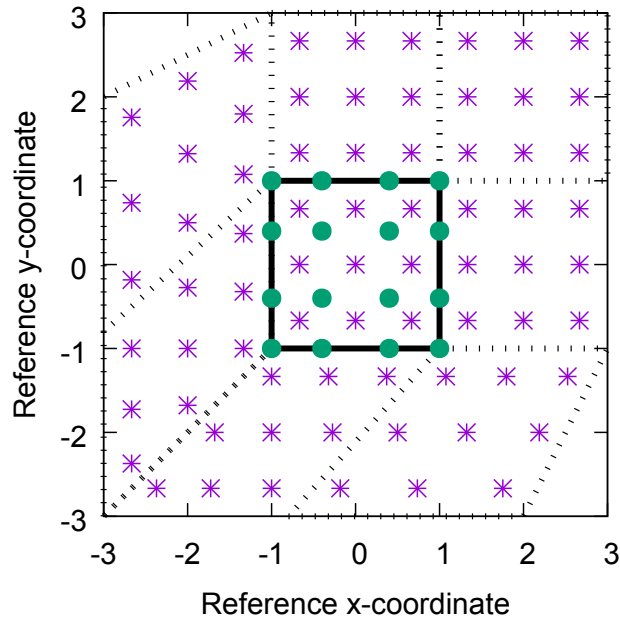
714 FIG. 10. Mean ω at two model levels in the middle troposphere, in a Held-Suarez configuration outfitted with
 715 real world topography. (Left) CAM-SE state on the GLL grid, *ne30np4*, (Middle) CAM-SE-CSLAM state on
 716 the GLL grid, *ne30np4* and (Right) CAM-SE-CSLAM state on the physics grid, *ne30pg3*. The ω fields are
 717 computed from a 1200 day Held-Suarez simulation. The data are contoured according to a ‘cell fill’ approach,
 718 in which the coupler grids (e.g., Figure 4) are used to delineate the vertices of the control volumes.



719 FIG. 11. Climatological total precipitation rate computed from the final 19 years of a pair of 20 year long
 720 AMIP type simulations. (Left) CAM-SE, (middle) CAM-SE-CSLAM and (Right) their differences. The differ-
 721 ence field is computed through bilinearly interpolating to a common latitude-longitude grid.



722 FIG. 12. Climatological total precipitation rate computed from the final 19 years of a suite of 20 year long
 723 AMIP simulations, using CAM-SE (ne30np4), CAM-SE-CSLAM (ne30np3) and CAM-FV (f09). The top plot
 724 is an observational product, the gridded GPCP climatological precipitation dataset.



725 FIG. 13. Schematic of the coordinate system in which the dimensionally split cubic Lagrange interpolation
 726 is computed. The physics grid centers are marked with asterisks and the GLL points, we are interpolating to,
 727 with solid filled circles. The element in which the GLL points are located is bounded by thick black lines and
 728 located in the lower left corner of a panel. The stippled lines mark the boundaries of the remaining elements.
 729 For simplicity we are using the normalized coordinate centered at the element on which the GLL points we are
 730 interpolating to are located. Note that the coordinates for points on neighboring panels (using a different local
 731 coordinate system) must be transformed to the coordinate system of the element in question.